The Astrophysical Journal, 713:25–31, 2010 April 10 doi:10.1088/0004-637X/713/1/25

DISTANCE TO MULTIPLE KINEMATIC COMPONENTS OF QUASAR OUTFLOWS: VERY LARGE TELESCOPE OBSERVATIONS OF QSO 2359–1241 AND SDSS J0318–0600

Manuel A. Bautista[1,2], Jay P. Dunn[1], Nahum Arav[1], Kirk T. Korista[2], Maxwell Moe[3], and Chris Benn[4]
[1] Department of Physics, Virginia Polytechnic and State University, Blacksburg, VA 24061, USA; manuel.bautista@wmich.edu
[2] Department of Physics, Western Michigan University, Kalamazoo, MI 49008-5252, USA
[3] Department of Astronomy, University of Colorado, Boulder, CO, USA
[4] Isaac Newton Group, Observatorio del Rogue de los Muchachos, Spain
Received 2009 November 13; accepted 2010 February 17; published 2010 March 16

ABSTRACT

Using high-resolution Very Large Telescope spectra, we study the multi-component outflow systems of two quasars exhibiting intrinsic Fe II absorption (QSO 2359–1241 and SDSS J0318–0600). From the extracted ionic column densities and using photoionization modeling, we determine the gas density, total column density, and ionization parameter for several of the components. For each object, the largest column density component is also the densest, and all other components have densities of roughly 1/4 of that of the main component. We demonstrate that all the absorbers lie roughly at the same distance from the source. Further, we calculate the total kinetic luminosities and mass outflow rates of all components and show that these quantities are dominated by the main absorption component.

Key words: galaxies: active – quasars: absorption lines – ultraviolet: galaxies

Online-only material: color figures

1. INTRODUCTION

Rest-frame UV spectra of roughly 20% of all quasars exhibit blueshifted broad absorption lines (BALs) that are indicative of an outflow. BALs are mainly associated with resonance lines of high-ionization species, such as C IV, N V, O VI (HiBAL), and can reach velocities as high as 50,000 km s^{-1} (Weymann 1995; Turnshek 1995). Despite various recent statistical studies of BAL quasars (Hall et al. 2003; Trump et al. 2006; Ganguly & Brotherton 2008), the relationship between HiBAL and the host galaxy remains illusive as these outflows do not contain distance diagnostics in their spectra. Thus, it is difficult to establish whether the outflows affect only the near active galactic nucleus (AGN) environment (0.1–10 pc) or they extend to the scales of the entire galaxy (1–10 kpc).

A subset of BALQSOs also shows absorption features from low-ionization species such as Mg II, Al II, and most importantly for diagnostics, Fe II and Si II. These absorption features are generally complex, as they are made of multiple components of narrower (of the order of a few hundred km s^{-1}) absorption troughs. AGNs with this kind of features are often referred to as FeLoBAL. In these systems, the spectra of Fe II and Si II are valuable because they often include absorption troughs from metastable levels, which serve to determine the distance of the outflow from the central source and thereby begin to relate the outflows to their host galaxy. Such outflows were studied in the past (Wampler et al. 1995; de Kool et al. 2001, 2002; Hamann et al. 2001; Arav et al. 2001). However, the presently available Sloan Digital Sky Survey (SDSS) and the development of advanced BAL analysis tools (Arav et al. 2002, 2005; Gabel et al. 2005) allow for a more accurate and systematic study of these systems. With this in mind, we began a comprehensive study of FeLoBAL outflows that contain distance diagnostics (Arav et al. 2008; Korista et al. 2008; Dunn et al. 2010; Moe et al. 2009).

Up to the present, though, all studies are based on either global properties of the multi-component absorption troughs or the strongest kinematic component. Little is known about the individual physical properties of the components and their relationship to the whole outflow. In the best-studied cases, Wampler et al. (1995) and de Kool et al. (2001, 2002) were able to obtain some column densities for individual components, but could neither diagnose the physical conditions of the components nor derive their relative distances. Simple assumptions that all components had similar physical conditions and that they have either constant speed or equal monotonic acceleration would lead to the conclusion that either the absorbers are scattered along a wide range of distances from the central source or they vary in age as a result of episodic ejections. But BAL systems in general are far from simple. Apart from a weak correlations between the absorber bulk velocities and bolometric luminosity of the AGN (Laor & Brandt 2002; Dunn et al. 2008; Ganguly & Brotherton 2008), no correlations have been found among velocity, width, ionization, or any other observable properties.

Recent high spectral resolution eschell observations of two quasars QSO 2359–1241 and SDSS J0318–0600 with the Very Large Telescope (VLT) have allowed us to study in detail the various independent components that compose their FeLoBAL. QSO 2359–1241 (VNSS J235953–124148) is a luminous ($M_B = -28.7$), reddened ($A_V \approx 0.5$) quasar at redshift $z = 0.868$ (Brotherton et al. 2001). SDSS J0318–0600 is also a highly reddened bright quasar ($A_V \approx 1$ and $M_B = -28.15$) at redshift $z = 1.967$. Both quasars exhibit a rich multi-component FeLoBAL comprising five and eleven components, respectively. The strongest components in the FeLoBAL, which are also the first absorbers from the central engine (see Section 3) for each of these objects, were measured and analyzed in Arav et al. (2008) and Korista et al. (2008) for QSO 2359–1241 and in Dunn et al. (2010) for SDSS J0318–0600. It was found that the absorbers are located at ∼3 kpc and between 6 and 20 kpc from the central engine, respectively.

QSO 2359–1241 and SDSS J0318–0600 are the first to be studied in detail from a sample of ∼80 FeLoBAL quasars with resonance and metastable Fe II absorption lines (FeLoBAL quasars) in their spectra. These lines can be used for direct determination of the physical conditions and energy transportation

Table 1
Measured Column Densities in QSO 2359–1241

Species	E_{low} (cm^{-1})	Column Density ($\times 10^{12}$ cm^{-2})				
		Comp. **a**	Comp. **b**	Comp. **c**	Comp. **d**	Comp. **e**
He I	159 856	14.3 ± 0.7	22.9 ± 3.4	6.1 ± 0.3	4.5 ± 2.2	138.0 ± 9.9
Fe II	0	0.49 ± 0.08	5.7 ± 1.5	2.7 ± 0.3	2.7 ± 0.1	72.4 ± 3.5
Fe II	385		0.93 ± 0.28	0.40 ± 0.09	0.60 ± 0.22	32.4 ± 1.2
Fe II	668		1.1 ± 0.5			18.2 ± 1.3
Fe II	863		0.45 ± 0.20			11.5 ± 0.9
Fe II	977					7.1 ± 0.6
Fe II	1873					77.6 ± 9.5
Fe II	7955					5.0 ± 0.5
Mg I	0	0.04 ± 0.02	2.1 ± 1.0	0.28 ± 0.02	0.04 ± 0.03	0.83 ± 0.06
Mg II	0					>65
Si II	0		198 ± 48			
Si II	287					794 ± 206
Al III	0			12.7 ± 0.4		>79
Ca II	0	0.07 ± 0.03	0.83 ± 0.04	0.47 ± 0.02		3.3 ± 0.3
Ni II	8394					6.2 ± 0.6

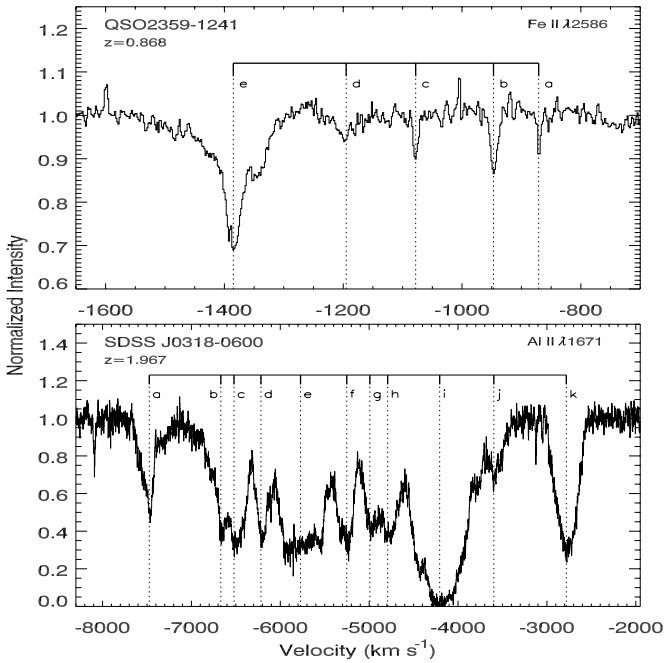

Figure 1. Absorption troughs showing five and 11 clearly separated absorption components in the spectra of QSO 2359–1241 and SDSS J0318–0600, respectively. The same components in velocity space seem to be present in all troughs of the same object.

of the outflows. The sample was extracted out of 50,000 objects in the SDSS database as part of a major ongoing effort to study the nature of quasar outflows and their effects on the host galaxy (Moe et al. 2009).

2. THE MEASURED COLUMN DENSITIES

Observations of QSO 2359–1241 and SDSS J0318–0600 consist of echelle VLT/UVES high-resolution ($R \approx 40{,}000$) spectra with 6.3 hr exposures for each object. Figure 1 illustrates the structure of the absorption troughs. The observations for QSO 2359–1241 were presented in Arav et al. (2008), together with the identification of all the absorption features associated with the outflow. Column densities of only the strongest component (*e*) were measured at that time. The observations of SDSS J0318–0600 are presented in Dunn et al. (2010). The high signal-to-noise data allowed us to measure the column densities from 5 unblended absorbers in QSO 2359–1241 and 11 components in SDSS J0318–0600. For the latter, though, only the strongest components, **a**, **i**, and **k**, could be independently measured, while all other components had to be measured as a single blended structure. Whenever possible, the column densities were determined through three different assumptions, i.e., full covering or apparent optical depth, partial line-of-sight covering, and velocity-dependent covering according to the power-law method of de Kool et al. (2001) and Arav et al. (2005). For each component in QSO 2359–1241, we find that the troughs require the power-law method to determine the full column density. We quote the column density determined by the power-law method in Table 1. For the three components in SDSS J0318–0600, we find that the results of these three methods are generally in good agreement, indicating that there is full covering of each source and the column densities could be reliably measured (see Dunn et al. 2010).

The measured column densities for the observed components in QSO 2359–1241 and SDSS J0318–0600 are given in Tables 1 and 2, respectively.

3. ANALYSIS OF SPECTRA AND MODELING

3.1. The Density of the Outflows

We use the observed ratios of column densities of excited to resonance lines as electron density indicators, which are directly proportional to the level populations. In QSO 2359–1241, we find excellent diagnostics from the Fe II column densities of the $a^5D_{7/2}$ level at 385 cm^{-1} and the ground level $a^5D_{9/2}$. The diagnostics are shown in Figure 2. From these, we get $\log(n_e/cm^{-3}) = 4.4 \pm 0.1$ for component **e** (see Korista et al. 2008), $\log(n_e/cm^{-3}) = 3.8 \pm 0.2$ for component **d**, and $\log(n_e/cm^{-3}) = 3.6 \pm 0.1$ and 3.6 ± 0.2 for components **c** and **b**. Unfortunately, we have no excited lines in component **a** suitable for diagnostics. The theoretical level populations for the Fe II ion were computed from the atomic model of Bautista & Pradhan (1998).

In SDSS J0318–0600, we find a density diagnostic for component **a** in the ratio of C II column densities of the excited level at 63 cm^{-1} ($^2P^o_{3/2}$) to the ground level ($^2P^o_{1/2}$), which yields $\log(n_e/cm^{-3}) = 2.6 \pm 0.2$ cm^{-3}. This is consistent with the

Table 2
Measured Column Densities in SDSS J0318–0600

Species	E_{low}(cm^{-1})	Column Density ($\times 10^{12}$ cm^{-2})			
		Comp. **a**	Comp. **i**	Comp. **k**	Comp. **b–h**
Al II	0	116.1 ± 0.1	400 ± 40	35.0 ± 0.3	>390
Al III	0	46.0 ± 0.4	1560 ± 220	73.0 ± 0.8	>810
C II	0	333 ± 11		1100 ± 200	>14000
C II	63	577 ± 21	>19000	1800 ± 300	
C IV	0	734 ± 10	29000 ± 3000	1297 ± 13	>10000
Fe II	0	<40	1275 ± 35	154 ± 6	>490
Fe II	385		294 ± 77		
Fe II	668			9.0 ± 0.3	
Fe II	863		147 ± 36		
Fe II	977				
Fe II	1873		163 ± 49		
Fe II	2430		25.0 ± 5.4		
Fe II	7955		8.1 ± 0.2		
Mg II	0	28.7 ± 0.1	3200 ± 400	192 ± 1	>880
Mn II	0		17.5 ± 0.1		
Ni II	0		180 ± 4	<120	
Ni II	8394		64.0 ± 0.4	10.0 ± 0.3	
Si II	0	101 ± 3	7220 ± 100	640 ± 150	>3500
Si II	287	<50	7380 ± 130	352 ± 12	
Si IV	0	145 ± 6	5600 ± 1300	140 ± 4	>1800

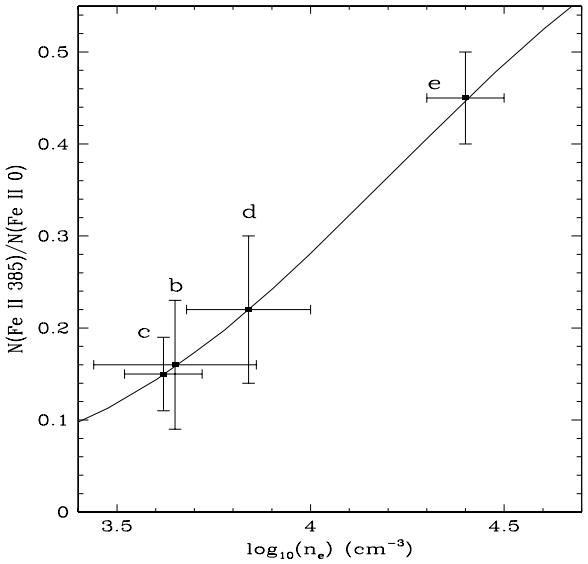

Figure 2. Electron density diagnostics from Fe II in QSO 2359–1241. The ratio of column densities of the excited level at 385 cm^{-1} ($a\,^6D_{7/2}$) to the ground level ($a\,^6D_{9/2}$) is plotted against the logarithm of the electron density. The measured ratios for each of the FeLoBAL components are drawn on top of the theoretical prediction. The uncertainties in the measured ratios are depicted by vertical bars, and that leads to uncertainties in the derived electron density which are indicated by horizontal bars.

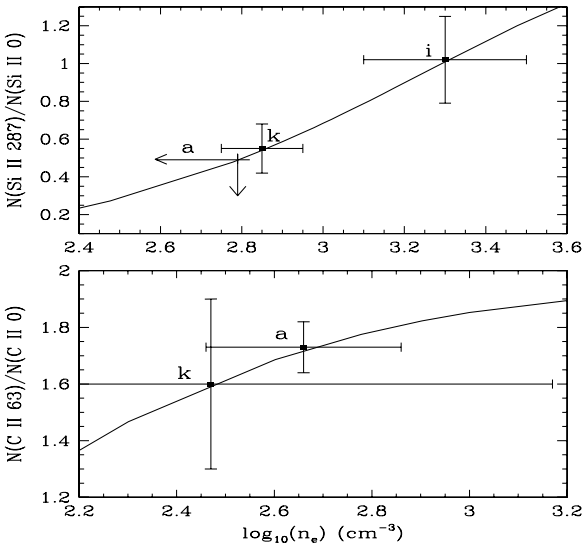

Figure 3. Electron density diagnostics from the observed ratios of column densities of excited to ground levels of C II and Si II in SDSS J0318–0600. For the component **a**, only an upper limit to the Si II ratio could be obtained from observations.

limit $\log(n_e/\mathrm{cm}^{-3}) < 2.8$ from the ratio of the Si II excited (287 cm^{-1}; $^2P^o_{3/2}$) to the ground ($^2P^o_{1/2}$) levels. For components **i** and **k**, the Si II ratios yield $\log(n_e/\mathrm{cm}^{-3}) = 3.3 \pm 0.2$ and $\log(n_e/\mathrm{cm}^{-3}) = 2.85 \pm 0.10$, respectively. Additional diagnostics from Fe II are available for component **i** and they are all consistent with the present determination (see Dunn et al. 2010). Figure 3 illustrates the present diagnostics. The theoretical level populations for C II were computed using the effective collision strengths of Blum & Pradhan (1992) and A-values from Wiese & Fuhr (1995). For the Si II spectral model, we use the effective collision strengths of Dufton & Kingston (1991) and A-values for forbidden transitions of Nussbaumer (1977).

In Arav et al. (2008), Korista et al. (2008), and Dunn et al. (2010), we showed that the troughs in QSO 2359–1241 and SDSS J0318–0600 arise from a region where hydrogen is mostly ionized, thus the electron density derived above should be nearly equal (within ∼10%) to the total hydrogen density of the clouds.

3.2. Ionization Structure of the Outflows

Under the premise that the absorbers are in photoionization equilibrium, we assume constant gas density clouds in plane parallel geometry. Thus, the ionization structure of a warm photoionized plasma is typically characterized by the so-called

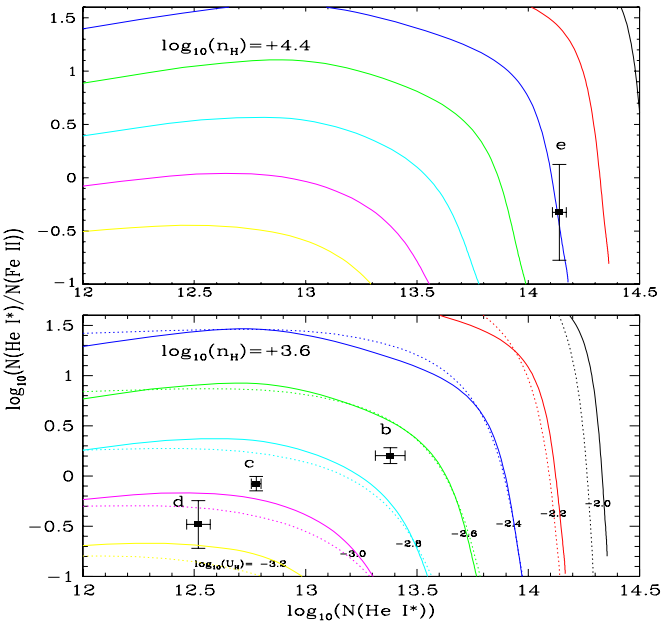

Figure 4. Results of grid models for QSO 2359–1241 and diagnostics of U_H and total column density for all the kinematic absorption components of the outflow. The various curves presented are for $\log_{10}(U_H) = -2.2$ (red), -2.4 (blue), -2.6 (green), -2.8 (cyan), -3.0 (magenta), and -3.2 (yellow). The solid lines depict the results from the MF87 SED and the dotted lines show the results from the spectrum transmitted through (attenuated by) component **e**. The calculated column densities are plot for three different values of n_H, in agreement with the previous density diagnostics.

(A color version of this figure is available in the online journal.)

ionization parameter, which is defined as

$$U_H \equiv \frac{\Phi_H}{n_H c} = \frac{Q_H}{4\pi R^2 n_H c}, \quad (1)$$

where c is the speed of light, n_H is the gas density, Φ_H is the ionizing photon flux, Q_H is the rate of hydrogen ionizing photons emitted by the ionizing source, and R is the distance from the ionizing source to the cloud. From this definition, Q_H can be estimated directly from the luminosity of the object and some knowledge of its Spectral Energy Distribution (SED).

Korista et al. (2008) and Dunn et al. (2010) constructed detailed photoionization models of the main components of QSO 2359–1241 and SDSS J0318–0600 and determined their physical conditions. But, modeling all the absorbing components of the outflow simultaneously opens a variety of new scenarios. Fortunately, the combined measurements of column densities for Fe II and He I in all of the components of QSO 2359–1241 and Si II and Si IV in the components of SDSS J0318–0600 allow us to constrain the ionization parameter of all of these components.

We use the photoionization modeling code CLOUDY c07.02.01 (Ferland et al. 1998) to compute grids of models in U_H for each value of n_H of interest. All models are calculated for N_H (total hydrogen column density) running from the inner phase of the cloud to deep into the ionization fronts (IF's) where the temperature drops to only a few thousand K. For QSO 2359–1241, we assumed solar abundances as in Korista et al. (2008). Then, the accumulated column densities of the metastable $2\,^3S$ excited state of He I (hereafter, He I*) and total Fe II were extracted out of the CLOUDY output files and plotted in Figure 4 as N(He I*)/N(Fe II) versus logN(He I*). These plots serve as direct diagnostics of U_H by marking the measured column densities on the plots. Further, the value of N_H is also readily available as there is a direct correspondence in each model between the accumulated total hydrogen column and the accumulated column density of all species.

The diagnostic power of the combined He I* and Fe II lines was explained in Korista et al. (2008). It was shown that the He I* column density is set by the He II column, which is bound to the H II fraction and the ionization parameter. This is because whenever helium is ionized, hydrogen with a much lower ionization potential must be ionized too. For any conceivable quasar ionizing continuum, recombination of He II to neutral He occurs simultaneously with recombination of H II to neutral H. This is shown in Figure 1 of Korista et al. (2008). On the other hand, the ionization fraction of Fe II across the ionization threshold is determined by charge exchange with hydrogen:

$$Fe^{++} + H^0 \rightleftharpoons Fe^{+} + H^{+}.$$

Thus, the column density of Fe II traces the column of neutral hydrogen and

$$\frac{N(\mathrm{He\,I^*})}{N(\mathrm{Fe\,II})} \propto \frac{N(\mathrm{H\,II})}{N(\mathrm{H\,I})} \propto U_H; \quad (2)$$

in other words, the measured ratio of column densities of He I* to Fe II serves as direct indicator of the average ionization parameter of the gas cloud. Within the cloud, whose depth, r, is expected to be much smaller than R, the U_H varies as

$$U_H(r) \propto \frac{e^{-\tau(r)}}{n_e}, \quad (3)$$

where τ is the optical depth to hydrogen ionizing photons, which is proportional to the column density of neutral hydrogen. Hence, at the inner phase of the cloud and for a large fraction of it, hydrogen is nearly fully ionized and τ remains small. Within this depth in the cloud, the ionization of the gas and hence the N(He I*)/N(Fe II) ratio is expected to remain roughly constant (see Figure 8 in Arav et al. 2001). Deeper in the cloud, a small decrease in the ionization of hydrogen leads to an increase in τ, which in turns reduces the number of ionizing photons right ahead and results in even lower hydrogen ionization. At this point, an IF develops and is accompanied by a quick drop of the N(He I*)/N(Fe II) ratio into the cloud or, equivalently, N(He I*). Furthermore, the N(He I*)/N(Fe II) versus N(He I*) plots shown in Figure 3 offer a complete diagnostic for U_H and the total hydrogen column density (N_H) for clouds of a given chemical composition.

Here, it is important to realize that as these plots are sensitive to the integrated flux of hydrogen ionizing photons, most of which ($\sim$ 90%) arise from the spectral region between 1 and 4 Ry in Quasar SED. Thus, the plots depend only little on the actual shape of the SED. This is illustrated in Figure 3 by showing the theoretical curves as calculated with the Mathews & Ferland (1987, MF87 hereafter) quasar SED and with the transmitted spectrum from the innermost component (**e**) of the outflow. That component **e** is the first absorber from the source in QSO 2359–1241 becomes apparent as this has the largest U_H dex and is also the densest; thus it is concluded from Equation (1) that it must have the smallest distance R among all components (see also the discussion below).

From the diagnostics in Figure 4, it results that component **e** has $\log(U_H) = -2.4$ for $\log_{10}(n_H/\mathrm{cm}^{-3}) = 4.4$. Component **d** with a density $\log_{10}(n_H/\mathrm{cm}^{-3}) = 3.8$ has $\log_{10}(U_H) \approx$

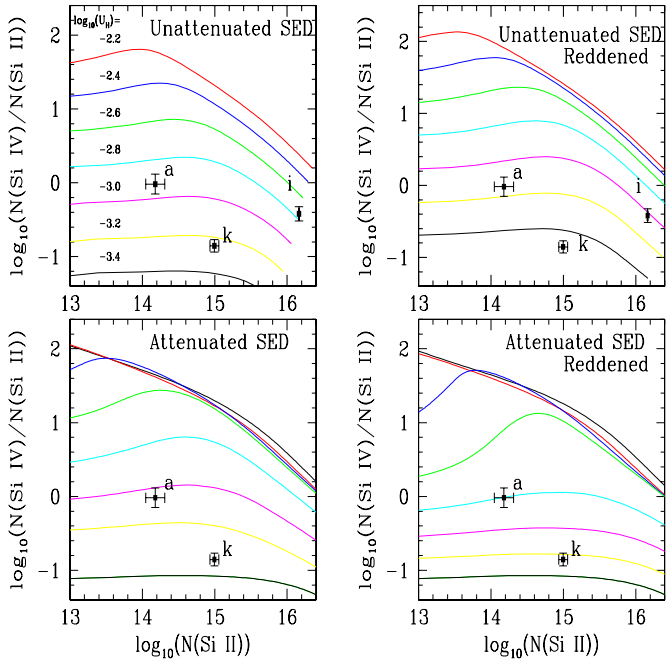

Figure 5. Results of grid models for SDSS J0318–0600 and diagnostics of ionization parameters and total column density for all kinematic absorption components of the outflow. The upper panels show the results with unattenuated unreddeneded SED (left panel) and reddeneded SED (right panel), while the lower panels present the results from the unreddened SED (left panel) and reddened SED (right panel) after attenuation by component **i**. All models we used $\log(n_H) = 3.0$, but are practically independent of n_H. The different colors of the curves correspond to $\log_{10}(U_H) = -2.2$ (red), -2.4 (blue), -2.6 (green), -2.8 (cyan), -3.0 (magenta), -3.2 (yellow), and -3.4 (black).

(A color version of this figure is available in the online journal.)

-2.8, and the two lowest density components **b** and **c** have $\log_{10}(U_H) \approx -2.7$ and -2.9, respectively. Note that the electron densities of components **b** and **d** are sufficiently similar to each other, and in fact overlap within the uncertainty bars. Then, it is appropriate to plot them on the same diagnostic diagram without any significant loss of accuracy.

We build similar plots for SDSS J0318–0600 but based on the column densities of Si II and Si IV (Figure 5). For these models, we start with a chemical composition expected for a galaxy with metallicity $Z = 4.2$, which we found to be a reasonable choice that fits well the measured column densities (Dunn et al. 2010). Models with either solar composition or very high metallicities (e.g., $Z = 7.2$) can be discarded on the basis of the observed absorption troughs for various species. Basing the diagnostics on two ions of the same element has two important advantages over the previous plots: (1) the column density ratio is mostly independent of the assumed chemical abundances, and (2) the plots are mostly independent of n_H. A disadvantage, though, is that the Si II is mostly created through photoionization by radiation below the hydrogen ionization threshold (0.6 Ry), while Si IV has a formation energy higher than that of He II. Consequently, the N(Si IV)/N(Si II) is more sensitive to the SED than in the previous case. Because SDSS J0318–0600 is a extremely reddened object and the location of the extinguishing dust with respect to the absorber is unknown, we need to consider two different SEDs for the models. These are the UV-soft SED developed in Dunn et al. (2010) and this SED after reddening. In Figure 4, we plot $\log(N(\text{Si IV})/N(\text{Si II}))$ versus $\log_{10}(N(\text{Si II})$ as obtained from the two SEDs considered (upper panel) and in the cases in which these SEDs are attenuated by component **i**, which is identified as the innermost absorber (lower panel).

From these diagnostics, the densest component **i** has the highest U_H ($= -2.75 \pm 0.10$ dex for the unreddened SED and 3.02 ± 0.10 dex for the reddened SED) and largest total column ($= 20.9 \pm 0.1$ dex for the unreddened SED and 20.1 ± 0.1 dex for the reddened SED). The lower density components **a** and **k** have considerably less column density and are less ionized.

From the physical conditions derived above, it is now possible to estimate the distance from each absorption component to the ionizing source. But, it is convenient to determine first the relative distances of all component to the source. The relative distance can be obtained more accurately from observations than absolute distance. This is because the absolute determination of distance depends strongly on the number of ionizing photons of the SED and on whether this is reddened before ionizing the cloud. So, we see that in QSO 2359–1241 and SDSS J0318–0600, the absolute distance to the absorbers varies by several factors depending on whether reddening of the SED occurs before or after ionizing the absorbers. This sort of uncertainty, however, does not affect the relative distances among absorbers. From Equation (1), one gets

$$\log(R/R_0) = \frac{1}{2}[\log(Q_H/Q_{H0}) - \log(n_H)/n_{H0}) - \log(U_H/U_{H0})], \quad (4)$$

where R_0, Q_{H0}, n_{H0}, and U_{H0} are the distance, rate of ionizing photons, particle density, and ionization parameter for a given reference component, which we choose as the strongest component in each of the absorbers studied (i.e., **e** in QSO 2359–1241 and **i** in SDSS J0318–0600). In identifying the innermost absorber, it is important to realize that in the first approximation that uses the same SED in determining the distance to all components the result is actually correct for the innermost component and overestimated for the rest (see Equation (4) of the manuscript). This means that the absorber with the shortest distance to the source in this first approximation is indeed the innermost absorber. For any other absorber to locate in the innermost position, the absorbers with shorter distance in the first order approximation would have to be at larger distances that initially estimated, which is impossible if the flux of ionizing photons is to be reduced by the effect of attenuation. Note that the relative locations of all the components could, in principle, be determined following the same logical argument, except that they are so close together that their estimated distance differences soon become smaller than the uncertainties. The strongest components are also the innermost, as we will see below. For any absorption component, that sees the same unattenuated radiation from the source as the reference component, $Q_H = Q_{H0}$. On the other hand, if a component is shadowed by intervening gas, particularly by the reference component, $Q_H < Q_{H0}$.

Table 3 presents the relative distance for components in the two absorbers considered. First, we assume that all components see the same unattenuated source ($Q_H = Q_{H0}$) and the results are given in columns 4 and 5 of the table. Under this assumption, components **e** and **i** are the innermost absorbers in QSO 2359–1241 and SDSS J0318–0600, respectively. Beyond these, other components are dispersed along 2–4 times that distance. We note that there are no correlations between velocity, n_H, and R.

However, given that the distance scales from the absorbers to the central source (kpc scales) are much greater than the size of the central source, it seems much more physically

Table 3
Calculated Distances to the Outflows

Comp.	v (km s^{-1})	δv (km s^{-1})[a]	$\log(n_H)$	Unattenuated SED		Attenuated SED[b]		$\log(N_H)$	$\dot{E}/\dot{E}_0$	$\dot{M}/\dot{M}_0$
				$\log(U_H)$	$\log(R/R_0)$	$\log(U_H)$	$\log(R/R_0)$			
				QSO 2359–1241						
b	−945	14 ± 5	3.65 ± 0.21	−2.68 ± 0.05	+0.5 ± 0.2	−2.68 ± 0.05	+0.0 ± 0.2	20.04 ± 0.07	0.10	0.21
c	−1080	30 ± 21	3.6 ± 0.1	−2.89 ± 0.05	+0.7 ± 0.1	−2.87 ± 0.05	+0.2 ± 0.1	19.46 ± 0.05	0.06	0.06
d	−1200	28 ± 12	3.84 ± 0.16	−2.83 ± 0.05	+0.5 ± 0.2	−2.81 ± 0.05	+0.0 ± 0.2	19.66 ± 0.05	0.08	0.11
e	−1380	59 ± 22	4.4 ± 0.1	−2.42 ± 0.03				20.56 ± 0.05	1	1
				SDSS J0318–0600, unreddened SED						
a	−7450	150 ± 10	2.65 ± 0.20	−3.04 ± 0.10	+0.5 ± 0.2	−3.02 ± 0.05	−0.3 ± 0.2	18.2 ± 0.2	0.01	0.004
i	−4200	670 ± 10	3.3 ± 0.2	−2.75 ± 0.10				20.9 ± 0.1	1	1
k	−2800	290 ± 10	2.85 ± 0.2	−3.30 ± 0.10	+0.5 ± 0.2	−3.40 ± 0.10	−0.2 ± 0.2	18.8 ± 0.3	0.002	0.005
				SDSS J0318–0600, reddened SED						
a	−7450	150 ± 10	2.65 ± 0.20	−3.13 ± 0.10	+0.4 ± 0.2	−2.80 ± 0.05	−0.2 ± 0.2	18.2 ± 0.2	0.07	0.02
i	−4200	670 ± 10	3.3 ± 0.2	−3.02 ± 0.10				20.1 ± 0.1	1	1
k	−2800	290 ± 10	2.85 ± 0.2	−3.40 ± 0.10	+0.4 ± 0.2	−3.19 ± 0.10	−0.1 ± 0.2	18.8 ± 0.3	0.01	0.03

Notes.
[a] Full width half maximum measured from Fe II in QSO 2359–1241 and Al II for SDSS J0318–0600
[b] The scales for QSO 2359–1241 and SDSS J0318–0600 are (R_0, $\dot{E}_0$, $\dot{M}_0$) = (1.3 ± 0.4 kpc, 2×10^{43} ergs s^{-1}, 40 $M_\odot$ yr^{-1}) and (6 ± 3 kpc, 1×10^{45} ergs s^{-1}, 180 $M_\odot$ yr^{-1}) if redning of the SED occurs before ionizing the outflow or (3 ± 1 kpc, 4×10^{43} ergs $^{-1}$, 100 $M_\odot$ yr^{-1}) and (18 ± 8 kpc, 6×10^{45} ergs s^{-1}, 1100 $M_\odot$ yr^{-1}) if redning occurs after.

plausible that the innermost components will shadow all further absorbers. Thus, as the first absorber is ionized by the source the next component in line from the source will only receive the transmitted SED from the first absorber, i.e., an attenuated SED. Furthermore, every component would only see SED attenuated by all absorbers closer to the source. Thus, in Table 3, we recalculate the distance for all components, other than the innermost, using SEDs that account for the attenuation by the innermost components. In this case, $\log(Q_H/Q_{H0}) = -1.0$ for QSO2359–1241 and −1.64 or −0.80 for SDSS J0318–0600 when using the unreddened and reddened SED, respectively. Surprisingly, all components of both objects converge, within the uncertainties, to the same distance from the central source. The uncertainties quoted in the table combine the errors in the values of n_H and N_H as diagnosed from the measured column densities from spectra. In both quasars studied here, the innermost absorbers are clearly identified as the densest and largest systems. The relative ordering of subsequent absorbers with respect to the central source could be tentatively estimated too, but we make no attempt to do so because the distance between them is always smaller than the uncertainties.

Also in Table 3, we present for every component the estimated kinetic luminosity and mass flux rate, defined as

$$\dot{E} = 4\pi\mu m_p \Omega R N_H v^3, \quad (5)$$

$$\dot{M} = 8\pi\mu m_p \Omega R N_H v, \quad (6)$$

were $\mu \approx 1.4$ is the mean particle mass for solar composition, m_p is the proton mass, and Ω is the global covering factor. For the present calculations, we adopt $\Omega = 0.2$ (see Section 4.2 in Dunn et al. 2010), which impacts the absolute values $\dot{E}_0$ and $\dot{M}_0$ given in the table but not the relative contributions of the components. These quantities are clearly dominated by the contribution of the largest innermost component of each outflow, while the minor components together contribute little to the total energy and mass carried out by the outflow. This indicates that the minor components may not be considered as ejection events in their own merits, but instead they are physically related to the main component.

Clearly, if attenuation of the SED were ignored, the distance to each of the minor components would be overestimated as well as their $\dot{E}$ and $\dot{M}$ contributions. Yet, even in this case, all the minor components together could only account for a small fraction of $\dot{E}$ and $\dot{M}$ sustained by the main component.

Finally, in Table 3, we quote the absolute values of R_0, E_0, and $\dot{M}_0$ for the main components of QSO 2350–1241 and SDSS J0318–0600 as obtained in Korista et al. (2008) and Dunn et al. (2010). These absolute value of R_0 is a lot more uncertain than the relative quantities tabulated here, for the reasons explained already at the beginning of this section. The determination of absolute kinetic energies and mass outflow rates are even more uncertain because they depend on R and the assumed valued for the global covering factor, which is the least-known parameter of the investigation.

4. DISCUSSION AND CONCLUSIONS

The high spatial resolution and signal-to-noise ratio of the VLT spectra allowed us to study the properties of each of the kinematic components in the FeLoBALS of quasars QSO 2350–1241 and SDSS J0318–0600. From the measurements of column densities for different kinematic components, we determined the electron number density for these components. For QSO 2350–1241, we used the ratio of column densities of Fe II from the excited level at 385 cm^{-1} and the ground level. In the case of SDSS J0318–0600, we used the ratios of column densities among levels of the ground multiplets of Si II and C II. Interestingly, there is a clear density contrast between the main kinematic component in each object and the smaller components. By contrast, all smaller components in each object seem to exhibit roughly the same density. The density contrast between the densest components and the smaller ones in each object is ∼ 0.8 dex for QSO 2350–1241 and ∼ 0.5 dex for SDSS J0318–0600.

Next, we determine the ionization parameters characteristic of each of the absorption components in both quasars. To this end, we designed diagnostic plots by which the ionization parameter as well as the total hydrogen column can be uniquely

determined. These plots demonstrate that: (1) any given ratio of column densities among medium and low ionization is a smooth function of the column density for a fixed value of the ionization parameter and (2) these curves of column density rations versus column density are monotonic with U_H. There are various consequences of this: (1) for a given pair of measured column densities (and fixed density, chemical composition, and SED), no more than one solution in U_H and N_H can be found; (2) U_H and N_H and their errors are necessarily correlated; (3) these solutions can be found either graphically or numerically in a way much more efficient than through generic numerical optimization techniques; and (4) the graphical nature of the diagnostic allows one to set the observations from various different observers on the same page and gain valuable insights.

In the determination of U_H and N_H, traditional plots of predicted column densities versus N_H as abscissa have various disadvantages. This is because for every column density measured there is whole family of solutions (U_H, N_H), thus both parameters must be determined simultaneously. A typical approach used is to normalize the predicted column densities to the measured columns and then look for the intersection between various curves. The disadvantages in this procedure is that dividing theoretical values by measured values mixes up theoretical and observational uncertainties. Further, a solution based on intersections of curves or broad regions offers no simple intuitive understanding of how the results may change in the case of systematic effects on either the theoretical modeling or the observations. By contrast, the plots that we propose here clearly allow one to visualize the error bars of the measurements and their significance relative to the predictions of different models. One can also visualize how systematic effects on the calculations, such as chemical composition or shape of the SED, would shift the results of the diagnostics. Another very important advantage of the proposed plots is the potential to put various kinematic components of the same trough on the same plot and compare them under equal conditions. It is true that the proposed plots do not show the resulting N_H explicitly, but by fixing U_H the whole problem is solved and there is a direct correspondence between the observed column density of observed species and N_H. Thus, N_H can be read directly from the tabulated solutions of the models.

We determined relative distances of the various kinematic components, under the assumption that all components see the same unattenuated SED. It becomes immediately clear that the component with the largest column density is always the first in line from the source. Once the first kinematic component in line was identified for each object, we include the effect of attenuation of the SED on the distance determination for the remaining components. It was found that distance determinations that ignore attenuation affects are significantly overestimated. By contrast, when attenuation by the innermost component is considered in the distance estimation, all the kinematic components in the absorption troughs are found in close proximity to each other, and possibly related. This result, if found generally true in most FeLoBAL, ought to have important consequences in our understanding of the dynamics and energetics of quasar outflows.

We acknowledge support from NSF grant AST 0507772 and from NASA LTSA grant NAG5-12867.

REFERENCES

Arav, N., Brotherton, M. S., Becker, R. H., Gregg, M. D., White, R. L., Price, T., & Hack, W. 2001, ApJ, 546, 140
Arav, N., Kaastra, J., Kriss, G. A., Korista, K. T., Gabel, J., & Proga, D. 2005, ApJ, 620, 665
Arav, N., Korista, K. T., & de Kool, M. 2002, ApJ, 566, 699
Arav, N., Moe, M., Costantini, E., Korista, K. T., Benn, C., & Ellison, S. 2008, ApJ, 681, 954
Arav, N., et al. 2007, ApJ, 658, 829
Bautista, M. A., & Pradhan, A. K. 1998, ApJ, 492, 650
Blum, R. D., & Pradhan, A. K. 1992, ApJS, 80, 425
Brotherton, M. S., Arav, N., Becker, R. H., Tran, H. D., Gregg, M. D., White, R. L., Laurent-Muehleisen, S. A., & Hack, W. 2001, ApJ, 546, 134
de Kool, M., Arav, N., Becker, R. H., Gregg, M. D., White, R. L., Laurent-Muehleisen, S. A., Price, T., & Korista, K. T. 2001, ApJ, 548, 609
de Kool, M., Becker, R. H., Gregg, M. D., White, R. L., & Arav, N. 2002, ApJ, 567, 58
Dufton, P. L., & Kingston, A. E. 1991, MNRAS, 248, 827
Dunn, J., Bautista, M. A., Arav, N., Korista, K. T., & Moe, M. 2010, ApJ, 709, 611
Dunn, J., Crenshaw, D. M., Kraemer, S. B., & Trippe, M. L. 2008, AJ, 136, 1201
Ferland, G. J., Korista, K. T., Verner, D. A., Ferguson, J. W., Kingdon, J. B., & Verner, E. M. 1998, PASP, 110, 761
Gabel, J. R., et al. 2005, ApJ, 623, 85
Ganguly, R., & Brotherton, M. S. 2008, ApJ, 672, 102
Hall, P. B., et al. 2003, ApJ, 593, 189
Hamann, F. W., Barlow, T. A., Chaffee, F. C., Foltz, C. B., & Weymann, R. J. 2001, ApJ, 550, 142
Korista, K. T., Bautista, M. A., Arav, N., Moe, M., Constantini, E., & Benn, C. 2008, ApJ, 688, 108
Laor, A., & Brandt, N. 2002, ApJ, 569, 641
Mathews, W. G., & Ferland, G. J. 1987, ApJ, 323, 456
Moe, M., Arav, N., Bautista, M. A., & Korista, K. T. 2009, ApJ, 706, 525
Nussbaumer, H. 1977, A&A, 58, 291
Trump, J. R., et al. 2006, ApJS, 165, 1
Turnshek, D. A. 1995, in QSO Absorption Lines, ed. G. Meylan (Berlin: Springer), 223
Wampler, E. J., Chugai, N. N., & Petitjean, P. 1995, ApJ, 443, 586
Weymann, R. J. 1995, in QSO Absorption Lines, ed. G. Meylan (Berlin: Springer), 213
Wiese, W. L., & Fuhr, J. R. 1995, NIST Database for Atomic Spectroscopy, Version 1.0, NIST Standard Reference Database 61 (Gaithersburgh, MD: NIST)